

## RESEARCH ARTICLE

# Primary wall cellulose synthase regulates shoot apical meristem mechanics and growth

Arun Sampathkumar<sup>1,‡</sup>, Alexis Peaucelle<sup>2,\*</sup>, Miki Fujita<sup>3,\*</sup>, Christoph Schuster<sup>4</sup>, Staffan Persson<sup>5</sup>, Geoffrey O. Wasteneys<sup>3</sup> and Elliot M. Meyerowitz<sup>6</sup>

## ABSTRACT

How organisms attain their specific shapes and modify their growth patterns in response to environmental and chemical signals has been the subject of many investigations. Plant cells are at high turgor pressure and are surrounded by a rigid yet flexible cell wall, which is the primary determinant of plant growth and morphogenesis. Cellulose microfibrils, synthesized by plasma membrane-localized cellulose synthase complexes, are major tension-bearing components of the cell wall that mediate directional growth. Despite advances in understanding the genetic and biophysical regulation of morphogenesis, direct studies of cellulose biosynthesis and its impact on morphogenesis of different cell and tissue types are largely lacking. In this study, we took advantage of mutants of three primary cellulose synthase (*CESA*) genes that are involved in primary wall cellulose synthesis. Using field emission scanning electron microscopy, live cell imaging and biophysical measurements, we aimed to understand how the primary wall *CESA* complex acts during shoot apical meristem development. Our results indicate that cellulose biosynthesis impacts the mechanics and growth of the shoot apical meristem.

**KEY WORDS:** Cell wall, Cell growth, Cellulose, Mechanics, Microtubules, Morphogenesis

## INTRODUCTION

A central question in developmental biology is how the growth and morphogenesis of cells, organs and organisms are controlled. Apart from genetic and hormonal inputs, plant cell morphogenesis is underpinned by irreversible changes in physical form or shape that are influenced by the laws of mechanics. Plant cells are subjected to different mechanical forces exerted by factors such as turgor pressure and by the growth of neighboring cells. Plant cell walls, the stiff yet malleable structures that bind plant cells, direct turgor-driven cell growth and shape and reinforce regions experiencing mechanical tension. The cell wall is also the major source of biomass on Earth and is used as a food, feed, fuel and fiber resource, highlighting its importance both for plant growth and for human society.

Primary cell walls, present around young expanding cells, comprise polysaccharides (cellulose, hemicelluloses and pectins) along with glycosylated proteins and solutes. Cell wall polysaccharides are formed either at the plasma membrane or in Golgi cisternae, from which they are secreted to the apoplast. Cellulose, a paracrystalline  $\beta$ -1,4-linked glucan polymer, acts as a scaffold for other polymers in the wall and is synthesized by CELLULOSE SYNTHASEs (*CESAs*), which exist as hexameric complexes at the plasma membrane. The *CESAs* move along the plasma membrane during synthesis as a result of their catalytic activity (McFarlane et al., 2014). This probably results from microfibril entrapment in the cell wall, such that further synthesis of cellulose forces the *CESA* complex to move. The *CESA* trajectories are often defined by the underlying cortical microtubule (MT) cytoskeleton (Paredez et al., 2006). Genetic evidence suggests that three different *CESAs*, *CESA1*, 3 and 6, are important for primary cell wall cellulose biosynthesis. A certain level of functional redundancy is observed between *CESA2*, 5 or 9 with *CESA6*, whereas the *CESA1* and 3 subunits are nonredundant and, therefore, are necessary for cellulose synthesis (Desprez et al., 2007; Persson et al., 2007). Nevertheless, characterization of the *CESA6*-like genes has also revealed subfunctionalization of *CESA* subunits during seed coat development (Mendu et al., 2011).

The shoot apical meristem (SAM) comprises a group of cells found at each shoot apex and is responsible for generating all the aboveground organs. A series of experiments demonstrated the existence of a causal loop in which tissue geometry and turgor-driven physical stresses regulate the alignment of MTs during SAM development (Hamant et al., 2008). The organization of the MT cytoskeleton is thought to regulate the deposition of cellulose microfibrils (CMF) during SAM development, which in turn would influence its morphology. These observations suggest a feedback mechanism between tissue morphology, MTs and cellulose synthesis at the SAM (Sampathkumar et al., 2014b).

Leaf and flower initiation at the SAM are proposed to be driven by the local accumulation of auxin, which promotes MT disorder and cell wall loosening (Sassi et al., 2014). These events are coupled with changes to the pectin methyl esterification status in the wall that allows for organogenesis at the SAM (Braybrook and Peaucelle, 2013). More recently, the expression of a suite of genes encoding 115 wall-synthesizing and/or modifying enzymes was mapped at the SAM, and the functional importance of the *CELLULOSE SYNTHASE LIKE D (CSLD)* gene family in SAM morphogenesis was demonstrated (Yang et al., 2016). Polysaccharide linkage analysis of cell wall material from the SAM revealed cellulose to be the most abundant polysaccharide, contributing ~30% of the total cell wall material. As expected, this correlated with high mRNA levels of several *CESAs*. Nevertheless, detailed functional studies of *CESAs* in the SAM are lacking, despite being assumed as a major contributing factor to the mechanics of the tissue. In this study,

<sup>1</sup>Max Planck Institute of Molecular Plant Physiology, Am Mühlenberg 1, 14476 Potsdam-Golm, Germany. <sup>2</sup>Institut Jean-Pierre Bourgin, INRA, AgroParisTech, CNRS, Université Paris-Saclay, 78000, Versailles, France. <sup>3</sup>Department of Botany, University of British Columbia, 6270 University Boulevard, Vancouver V6T 1Z4, Canada. <sup>4</sup>Sainsbury Laboratory, University of Cambridge, Cambridge CB2 1LR, UK. <sup>5</sup>School of Biosciences, University of Melbourne, Parkville, VIC 3010, Australia. <sup>6</sup>Howard Hughes Medical Institute and Division of Biology and Biological Engineering, 1200 East California Boulevard, Pasadena, CA 91125, USA.

\*These authors contributed equally to this work

‡Author for correspondence (sampathkumar@mpimp-golm.mpg.de)

© A.S., 0000-0003-1703-0137

we used an interdisciplinary approach to evaluate the role of the CESA complex in influencing both physical and biological processes at the SAM.

## RESULTS

### Cellulose microfibril patterns are similar to microtubule organization at the shoot apical meristem

MT organization at the SAM has been used as a proxy for CMF patterns (Hamant et al., 2008; Sampathkumar et al., 2014a). Live cell-imaging approaches have been used to visualize CESA complexes in hypocotyl cells, trichomes, seed coat epidermal cells and protoxylem cells (e.g. Paredes et al., 2006; Yanagisawa et al., 2015; Griffiths et al., 2015; Watanabe et al., 2015). These studies suggested that CESA complex dynamics and spatial distribution are regulated differentially based on cell type and developmental stage. However, this technique is challenging at the

SAM and we were unable to acquire live images of fluorescently labeled CESAs at sufficient resolution and fluorescence intensity to perform useful analyses in the SAM. Therefore, we resorted to field emission scanning electron microscopy (FESEM) of cryo-planed SAM tissue to survey newly deposited CMF arrangements in different domains (Fujita and Wasteneys, 2014). The small size of the SAMs in wild-type plants makes it difficult to prepare samples for FESEM; therefore, we opted for *clv3-2* mutants, which have substantially enlarged SAMs. The SAMs of *clv3-2* mutants display varying degrees of phenotypic severity compared with the wild type but still maintain a dome-like structure, compared with mutants of *clv1*, which have fasciated SAMs (Schoof et al., 2000). We observed many pit fields, as previously reported in young developing cells. FESEM revealed a dense network of fiber-like structures reminiscent of CMF in the innermost region of the cell wall, consistent with findings in other tissues (Fig. 1; Fujita and

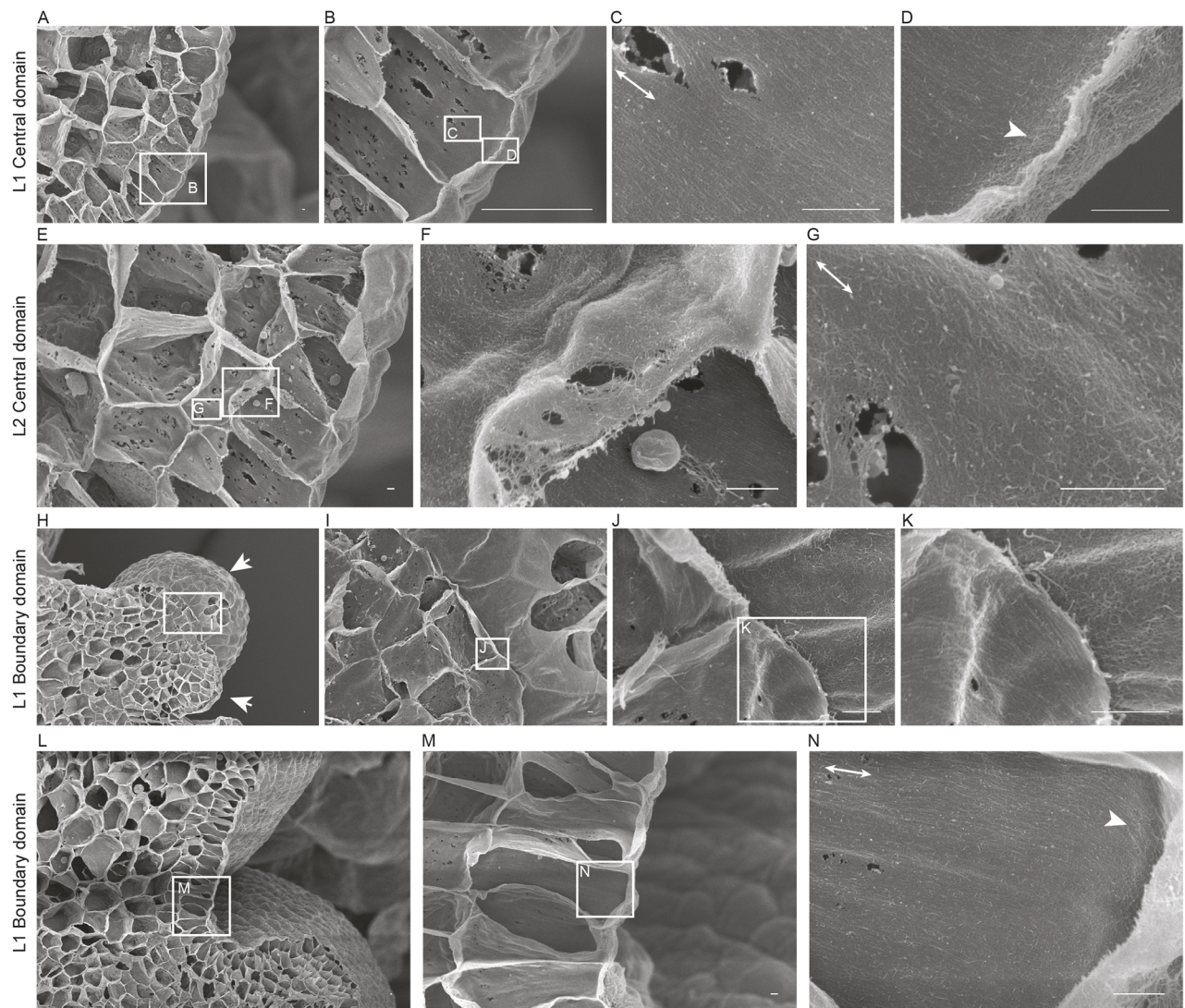


**Fig. 1. FESEM of cellulose microfibril orientation in the SAM.** Longitudinal section of the cell walls of the central domain of a SAM after removal of the membrane and cytoplasm, as viewed by FESEM (A-G). Sequentially enlarged images are indicated by rectangular boxes. Well-ordered CMF arrays along the longitudinal axis were observed in the inner face of the anticlinal wall of L1 layer (C). The arrowhead indicates disorganized CMF arrays observed along the inner periclinal face of cells in the L1 layer (D). CMF arrays deeper in the meristem (E). L2 layer showing CMFs with variable alignment in inner periclinal (F) and anticlinal walls (G). A longitudinal section parallel to the boundary domain of the SAM (H-K). Well-ordered CMF arrays along the long axis of the cell in the inner periclinal face of L1 layer (J-K). Arrows indicate young and older primordia. Longitudinal section at 90° through the boundary domain (L-N). Highly organized CMF array along the longitudinal axis of the inner anticlinal wall extends into the periclinal face, as indicated by the arrowhead (N). White lines with double arrows represent the longitudinal axis of the cell. Scale bars: 500 nm.



Wasteneys, 2014; Sugimoto et al., 2000). The inner face of the outer periclinal wall in the central zone cells of the L1 layer showed erratically organized CMFs in agreement with the reported MT distribution (Fig. 1D, Figs S1C,S2C; Hamant et al., 2008). We found a sharp transition from arbitrary CMF alignment in the inner periclinal wall to highly ordered CMF in the anticlinal wall (Fig. 1C, Fig. S2A,B). Orthogonal confocal microscope images of a fluorescent MT reporter [microtubule-binding domain Green Fluorescent Protein (MBD GFP); Marc et al., 1998] along the anticlinal walls showed a similar MT organization (Fig. S1E). The L2 layer cells in the meristem central zone contained erratic CMF alignments in the periclinal walls (Fig. 1E,F). The pattern of CMFs was consistent with that of the MTs in the periclinal wall of the L2 cells (Fig. S1D). CMFs along the L2 anticlinal walls, although having a general alignment along the longitudinal axis of the cells, did not exhibit as high a degree of anisotropic alignment as the CMFs in the L1 cells, whereas L2 anticlinal MTs did show a highly ordered organization (Fig. 1G, Figs S1F,S2D-F). The MT arrays in the epidermal cells of the boundary domain between floral primordia and the meristem exhibited a supracellular pattern of highly ordered MTs (Fig. S1B). The CMFs were also highly aligned on the periclinal wall, which forms a continuum with the anticlinal walls, at which a hyperparallel distribution of CMFs was observed (Fig. 1H-N). Hence, there was strong agreement between the ordering of MTs and CMFs in the L1 layer cell and in periclinal L2 walls, but less agreement between the observed MT and CMF patterns in anticlinal L2 walls of the SAM.

### **CESA1 and CESA3 are expressed differentially in the shoot apical meristem**

*CESA1* and *CESA3* were identified as the two most highly expressed *CESA* genes in the SAM (Yang et al., 2016). Transcripts of *CESA1* and *CESA3* are present throughout the SAM based on *in situ* hybridization experiments (Yang et al., 2016). However, because of high sequence similarities between the different *CESAs*, *in situ* hybridization to RNA fails to differentiate fully between different *CESA* gene products. To obtain detailed cellular level information and visualize spatial differences in the expression of these two genes, we generated transcriptional reporters of *CESA1* and *CESA3* by fusing a fluorescent protein with a nuclear targeting sequence behind the upstream genomic regions of the genes (4.5 kb and 3.2 kb upstream of the start codon of *CESA1* and *CESA3*, respectively). We also included 1.5 kb downstream of the stop codon of the genes that we placed at the 3' side of the coding sequence of the fluorescent protein. We observed that the *CESA1* promoter was active throughout the entire SAM, with higher activity in the rib meristem (Fig. 2A,B). The *CESA3* promoter also drove expression ubiquitously in the SAM but displayed the highest activity in L1 cells (Fig. 2C,D). These observations indicated that the *CESA1* and *CESA3* genes were abundantly expressed in the SAM and that there were differences in the spatial expression patterns of the two *CESA* genes.

### **Primary wall cellulose synthase mutations influence shoot apical meristem size and curvature**

To investigate the role of different primary wall *CESA* genes in the development of the SAM, we examined SAM phenotypes in mutants of *cesa1* and *cesa3* genes. The null mutants of *cesa1* and *cesa3* genes are pollen defective (Persson et al., 2007); therefore, we opted for the point mutants *cev1* (G617E) for *CESA3* and *any1* (D604N) for *CESA1*, which both have compromised cellulose synthesis (Ellis et al., 2002; Fujita et al., 2013). Given that *CESA6* is

considered a major contributing subunit of the primary wall *CESA* complex, we also included the *CESA6*-null mutant *prc1-1* in our analysis (Fagard et al., 2000). However, it is important to note that *CESA6* is expressed at moderate levels in the SAM (Yang et al., 2016). We observed that, whereas the SAM of *prc1-1* was similar to that of the wild type, the SAMs were significantly smaller in size in *any1* and *cev1* (Fig. 2E,G;  $P < 0.0001$ , Welch's *t*-test). Segmentation and quantification of individual surface areas of central zone cells revealed no significant changes in cell size, suggesting that the reduction in SAM size was a consequence of fewer cells in the mutant meristems (Fig. 2E, Fig. S3;  $P > 0.1$ , Welch's *t*-test). Extraction of surface geometry revealed a significantly higher degree of positive Gaussian curvature at the apex of the SAM in the *any1* and *cev1* mutants compared with wild type (Fig. 2F,H;  $P < 0.0001$ , Welch's *t*-test). SAM size and shape can influence phyllotactic angles, with smaller meristems having a more confined angle centered around  $137^\circ$  (Landrein et al., 2015). Quantification of postmeristematic phyllotactic patterns between successive silicles along the stem of these mutants showed marked changes in the distribution of the divergence angle (Fig. S4). Consistent with the previous finding by Landrein et al., 2015, we observed that the smaller SAMs of *any1* and *cev1* mutants showed a more robust phyllotactic pattern compared with wild type and *prc1-1*. To observe whether transient perturbation of cellulose would result in morphological abnormalities, we treated the SAM with either isoxaben, a known inhibitor of cellulose synthesis, or cellulase enzyme, which cleaves cellulose in the wall. However, within 75 h after isoxaben or cellulase treatment, we observed no major differences in the morphology of the SAM or with emerging primordia ( $n=10$  SAMs; Fig. S5A-D). By contrast, the emerging sepal cells of young flowers were swollen in two out of the ten SAMs treated with isoxaben, possibly because of the increased expansion rates observed in sepal primordia compared with the SAM (Fig. S5A,C). Similar changes were observed in cellulase-treated SAMs (Fig. S5D). It should be noted that the cellulase could act also on other polymers in the wall because its activity is not fully specific to cellulose. These results indicate that perturbations of cellulose by genetic means results in reduced SAM size and curvature.

### **Disruption of cellulose synthesis results in reduced cell wall stiffness**

To assess the contribution of cellulose to the mechanical properties of the cell wall at the SAM, we probed the surface of freshly dissected SAMs of the three different *cesa* mutant genotypes with an atomic force microscope (AFM). All *cesa* mutants showed a reduction in the mean cell wall stiffness in the anticlinal wall of the mutants compared with the wild type (Fig. 3A-F; *any1*,  $P=4.8\text{e-}3$ ; *cev1*,  $P=7.1\text{e-}3$ , Student's *t*-test). Despite having identical SAM size to that of the wild type, the *prc1-1* mutants still exhibited a reduction in cell wall stiffness ( $P=1.03\text{e-}3$ , Student's *t*-test). To further corroborate these results, we treated dissected SAMs with isoxaben for 24 h on plates containing growth medium. The SAMs were then probed with an AFM. SAMs cultured on media without isoxaben showed an overall reduction in stiffness compared with freshly dissected and probed SAMs. Despite this, the isoxaben-treated SAMs displayed a significant further reduction in elastic moduli of the anticlinal walls compared with the mock treatment ( $P=1.1\text{e-}7$ , Student's *t*-test) (Fig. 3G-K). Similar reductions in elastic modulus were observed in SAMs treated with cellulase ( $P=3.1\text{e-}4$ , Student's *t*-test) (Fig. 3G-K). These observations indicate that mutations and agents that perturb CMF biosynthesis and structure result in reduced cell wall stiffness at the SAM.

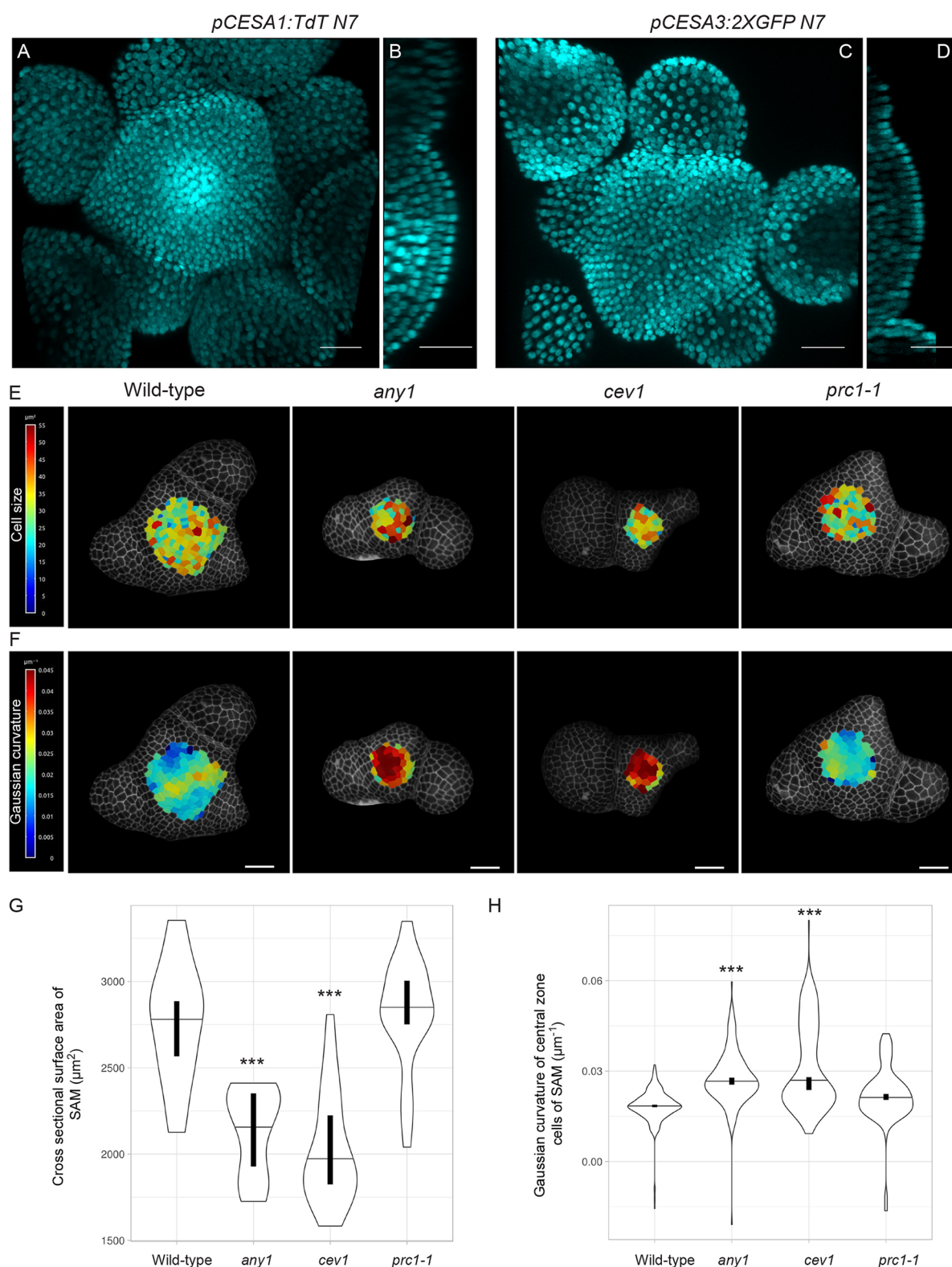


Fig. 2. See next page for legend.

### Perturbation of cellulose biosynthesis influences microtubule organization without impacting microtubule reorientation dynamics

We next tested whether the reduced cellulose levels and cell wall stiffness in the SAM could interfere with the ability of the cells to read

and respond to changes in their mechanical status. Given that MTs are one of the best-established components in stress-mediated mechanical feedback, we used MT alignment as a readout for the ability of cells to perceive mechanical signals. Isoxaben treatment induced hyperalignment of MTs in the SAM and epidermis of cotyledons



**Fig. 2. CESA activity impacts SAM development.** Maximum intensity projection of (A) *pCESA1:TdT N7* and (C) *pCESA3:2XGFP N7* and their respective orthogonal views (B,D). Cyan indicates nuclear fluorescence. L1 layer projections of representative SAM of wild-type plants, and *any1*, *cev1* and *prc1-1* mutants with the heat map of (E) the segmented cell surface area and (F) Gaussian curvature of cells in the central zone. (G) Violin plot reflecting the distribution of the cross-sectional surface area of cells in different genotypes (wild type  $n=22$ , *any1*  $n=20$ , *cev1*  $n=22$  and *prc1-1*  $n=26$  SAMs). (H) Violin plot showing Gaussian curvature distribution of central zone cells of different genotypes ( $n$ =cells/SAMs: wild type  $n=337/3$ , *any1*  $n=195/3$ , *cev1*  $n=163/4$  and *prc1-1*  $n=149/3$ ). Horizontal lines in violin plots indicate the median, whereas vertical bars indicate the 95% confidence interval for each median determined by bootstrapping. \*\*\* $P<0.0001$  (Welch's  $t$ -test). Scale bars: 25  $\mu$ m.

(Heisler et al., 2010; compare Fig. S5E,F). Such a response was also observed in cells treated with cellulase (Fig. S5G), indicating that both types of transient perturbation result in changes to the MT cytoskeleton. We observed MT organization in the *cev1* mutant SAM and quantitatively assessed MT ordering using FibrilTool (Boudaoud et al., 2014). This revealed a significant decrease in MT anisotropy in SAMs of the *cev1* mutant compared with the wild type (Fig. 4A-E). To determine the domain of the SAM from which such differences arise, we compared MT anisotropy in the central zone cells versus the boundary domain cells and noticed a significant drop in anisotropy only in the central zone cells of the *cev1* mutant (Fig. 4F;  $P<0.01$ , Welch's  $t$ -test). We further perturbed the mechanical stresses of the SAM by ablating small groups of cells in the center of the SAM and monitored the MT response in both wild type and *cev1*. The MTs in both genotypes responded in a similar fashion, gradually increasing in anisotropy around the ablated region on a similar timescale (Fig. 4G,H; Pearson correlation  $r=0.93$ ; Welch's  $t$ -test  $P=0.6$ ). These results indicate that perturbation of cellulose synthesis influences MT ordering at the SAM, but that the dynamics of MT reorientation was similar to the wild type in response to changes in mechanical stress.

### Impairment of cellulose synthesis impacts auxin efflux carrier protein PIN1 levels

The plant hormones auxin and cytokinin have a major role in regulating SAM morphogenesis and development. To evaluate whether the changes in SAM size of the *cesa* mutants were a consequence of disrupted hormone status at the SAM, we first monitored the distribution of the auxin efflux carrier protein PIN1 using *pPIN1:PIN1-GFP* in the *cev1* mutant. PIN1-GFP was localized in a polar fashion on the plasma membrane (Fig. 5A,B) toward domains of incipient primordia of the *cev1* mutant, similarly to the wild type (Fig. 5C,D). However, measurement of the total fluorescence intensity of cells in the central zone and incipient primordia showed a significant reduction in PIN1 signal in both domains compared with wild-type cells (Fig. 5C;  $P<0.01$ , Welch's  $t$ -test). Second, we used the cytokinin reporter *pTCS:GFP* to monitor cytokinin response in the *cev1* mutant. No difference in signal intensity was observed in the cells of mutant SAM compared with wild type (Fig. S6;  $P>0.7$ ; Welch's  $t$ -test), indicating that *cesa* mutations had no impact on cytokinin status at the SAM.

### Cellulose synthesis influences shoot apical meristem size by regulating cell growth

Next, to test whether cell cycle progression was perturbed in the different cellulose synthase mutants we performed *in situ* hybridization on SAM sections with a *HISTONE H4* antisense RNA probe (Fig. 6A). From this, we quantified the results of the *in situ* hybridization and calculated the mitotic index of the SAM (Geier et al., 2008). We observed a significant reduction in the index

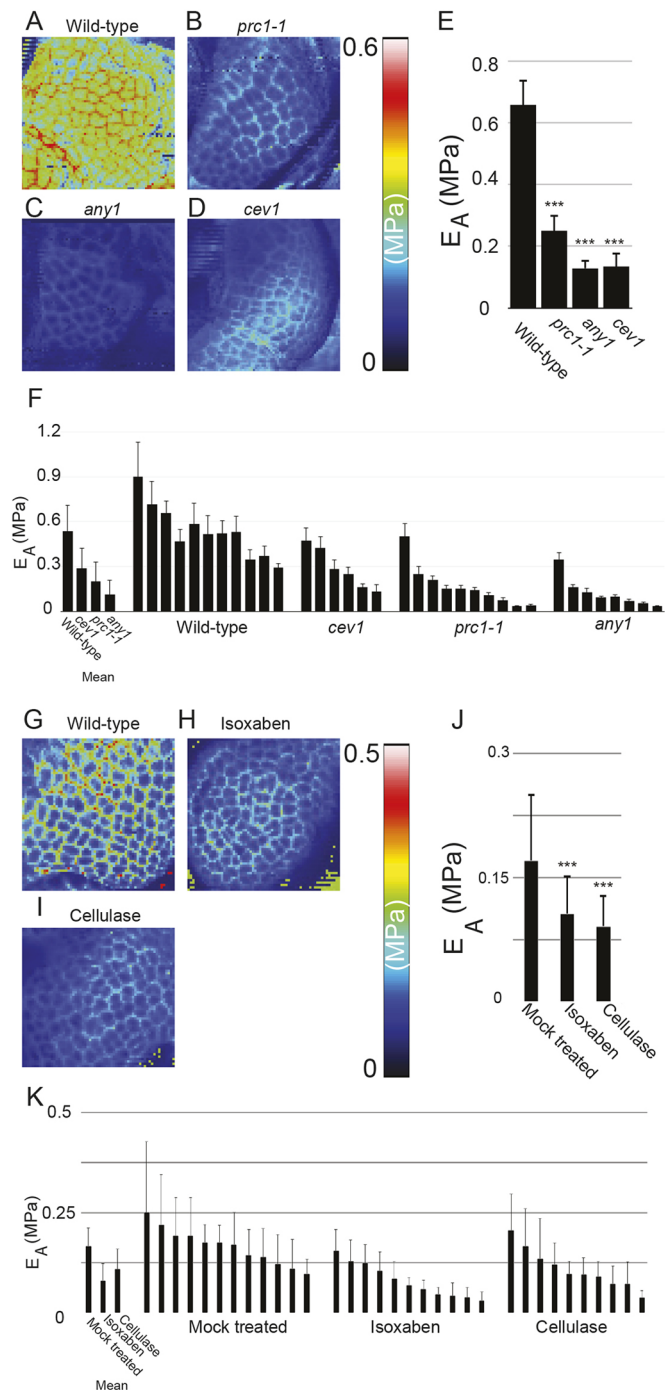


**Fig. 3. Disruption of cellulose synthesis impacts mechanical aspects of SAM.** Apparent Young's modulus ( $E_A$  or stiffness) map of the central domain of freshly dissected SAM of (A) wild type, (B) *prc1-1*, (C) *any1* and (D) *cev1*. (E) Histogram showing  $E_A$  of the respective SAM represented in A-D. (F) Mean  $E_A$  of SAMs of all genotypes along with individual meristem measurements. Apparent Young's modulus ( $E_A$  or stiffness) map of the central domain of SAMs that were cultured on growth media and then mock-treated (G), treated with isoxaben 40  $\mu$ M (H), or treated with 0.1% cellulase (I) for 24 h. (J) Histogram showing  $E_A$  of the respective SAMs represented in G-K. Mean  $E_A$  of SAMs of all genotypes along with individual meristem measurements (K). \*\*\* $P<0.0001$  (Student's  $t$ -test). Error bars show s.d. in all cases.

in both *any1* and *cev1* mutants (Fig. 6B;  $P<0.01$ ). These data were consistent with the reduced growth of the SAM in both *cev1* and *any1* (Fig. 2). This reduction in growth of cells could impact the

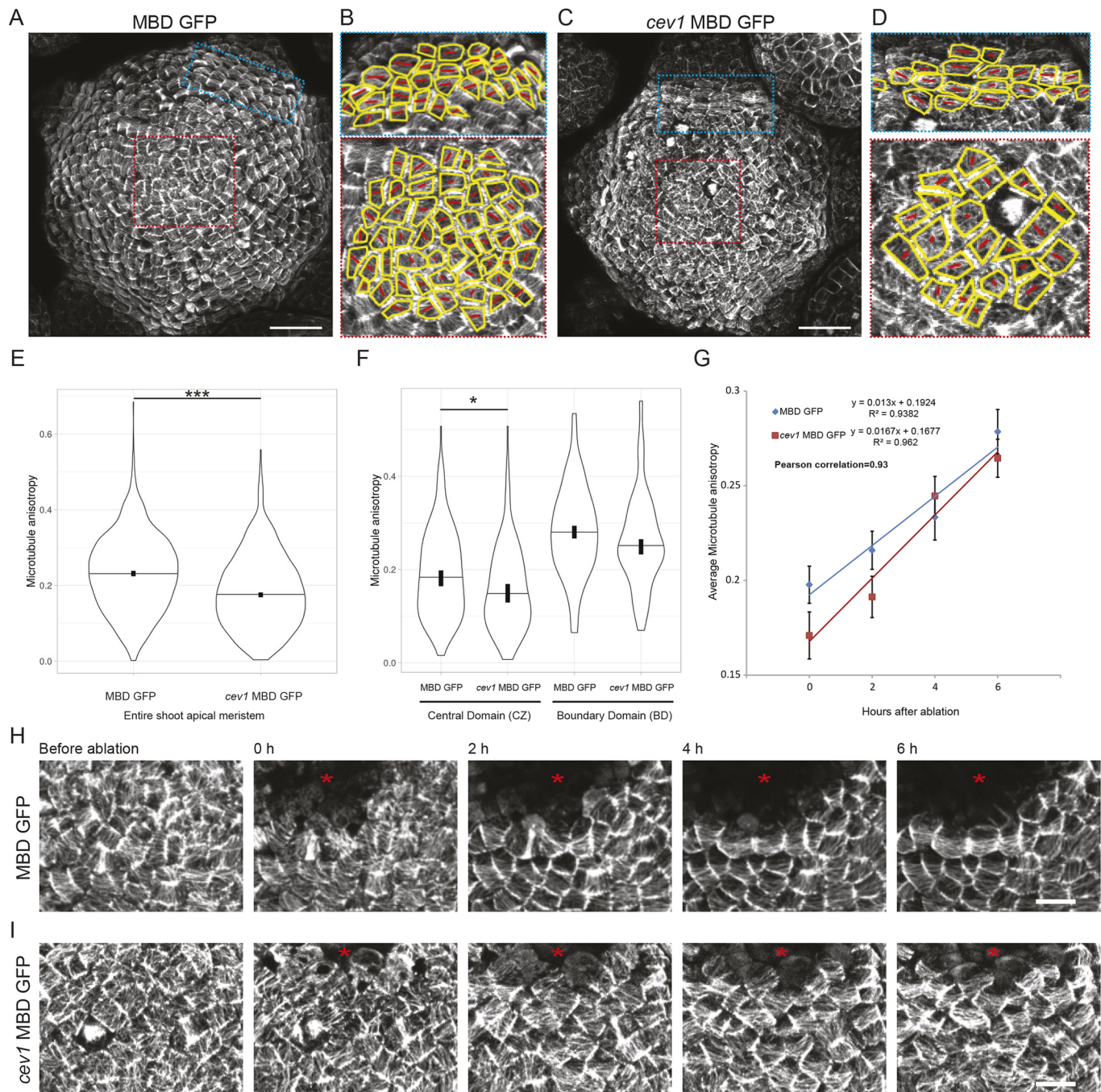


**Fig. 4. Impact of cellulose disruption on MT order in the SAM.** MT organization in the L1 layer of (A) MBD GFP and (C) *cev1* MBD GFP. (B,D) Manually segmented cells of both boundary and central zone cells in (A) and (C), respectively, with outline in yellow and red tensors indicating the major alignment of MTs within each cell, with the length of the line representing the degree of anisotropy (small to large represent lower to higher degrees of MT anisotropy), as measured from the images using FibrilTool. Violin plots showing distribution of MT anisotropy in (E) all cells ( $n$ =cells/SAMs: MBD GFP=1505/4 and *cev1* MBD GFP=1430/5) or (F) in cells of the central zone ( $n$ =cells/SAM, MBD GFP=216/4 and *cev1* MBD GFP=149/5) and the boundary domain ( $n$ =cells/SAM, MBD GFP=127/4 and *cev1* MBD GFP=95/4) (F) of the SAM. (G) Regression showing the change in mean MT anisotropy of the same group of cells over time after mechanical perturbation ( $n$ =cells/SAM, MBD GFP=80/4 and *cev1* MBD GFP=79/5 for each time point; error bars show s.e.m.). Changes in MT organization after ablation in (H) MBD GFP and (I) *cev1* MBD GFP. The red asterisk indicates the ablated region. Horizontal lines in violin plots indicate the median, vertical bars indicate for each median the 95% confidence interval determined by bootstrapping. \* $P$ <0.01, \*\*\* $P$ <0.0001 (Welch's  $t$ -test). Scale bars: 25  $\mu$ m in A-D and 5  $\mu$ m in H,I.

process of organogenesis at the SAM in the mutants. To assess this, we quantified the number of newly formed primordia each day for a period of 5 days in the *cev1* mutant. Consistent with the prediction, we found a reduced rate of organ emergence in the *cev1* mutant (Fig. 6C), which resulted in a significant increase in plastochron

compared with the wild type (Fig. 6D;  $P$ <0.0001; Welch's  $t$ -test). To further investigate the importance of cellulose synthesis in the regulation of SAM growth, we generated a double mutant between *cev1* and *clv1-8*, a mutant of the transmembrane receptor kinase CLAVATA1 that has a fasciated SAM with a greatly increased



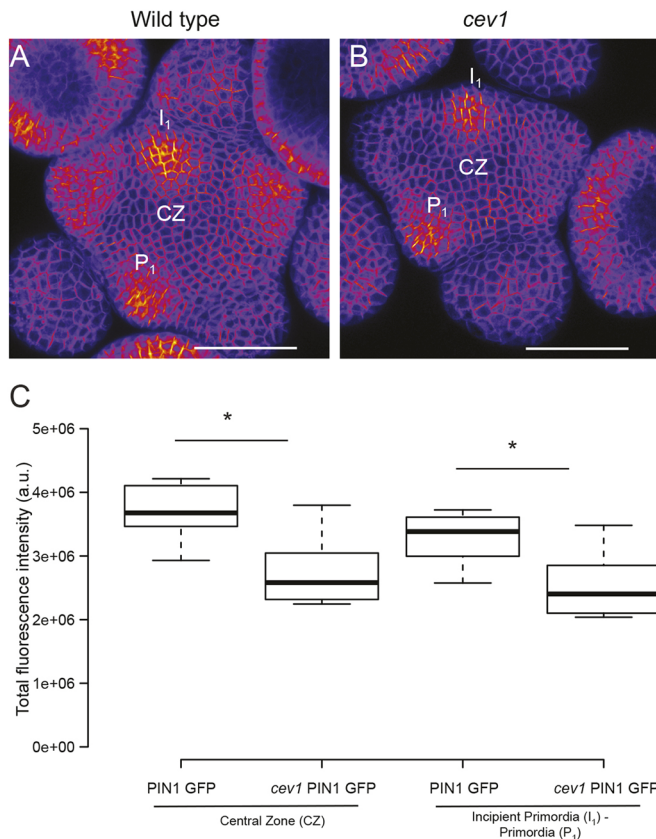


**Fig. 5. Auxin status in wild-type and *cev1* mutant meristems.** Sum intensity projection of *pPIN1:PIN1-GFP* in wild type (A) and *cev1* (B). Box plots of total fluorescence intensity obtained from cells of the central zone CZ (enclosure 25- $\mu$ m radius) and cells in incipient primordium I<sub>1</sub> or primordium P<sub>1</sub> (enclosure 12.5- $\mu$ m radius) (C) (wild type  $n=10$ , *cev1*  $n=8$  for both CZ and primordia). Center lines in box plots show the medians; box limits indicate the 25th and 75th percentiles as determined by R software; whiskers extend 1.5 times the interquartile range from the 25th and 75th percentiles. \* $P<0.01$  (Welch's *t*-test). Scale bars: 50  $\mu$ m in A,B.

number of cells. The *cev1* mutant was able to suppress the fasciated SAM phenotype of the *clv1-8* mutant (Fig. 6E;  $n=6$  out of 18 SAMs). These results indicate that cellulose synthesis has an important role in influencing SAM growth.

## DISCUSSION

The SAM generates all aboveground organs and thereby supports plant morphology from the onset of growth. Several regulatory networks that underpin the organization of the SAM have been investigated (Barton, 2010). However, how these networks support SAM growth based on structural elements of the cell, such as the cell wall, is largely unknown. Indeed, a mechanistic understanding of morphogenesis at the SAM requires proper knowledge of cell wall biosynthesis. In this study, we focused our efforts on deciphering the functional contribution of primary wall cellulose biosynthesis to the growth and development of the SAM.

Quantitative assessment of cell wall polymers in the SAM has shown that cellulose is the most abundant polymer (Yang et al., 2016). This was supported by high levels of *CESA1* and *CESA3* transcripts, detected by both RNA sequencing and *in situ* hybridization. *In situ* hybridization of *CESA1* and *CESA3* mRNA showed that they were expressed throughout the SAM with no absolute spatial differences. Our results, using *CESA* promoter

fusions with fluorescent proteins, did indicate subtle spatial differences in the expression of *CESA1* and *CESA3*. These differences could be linked to changes in cellulose deposition at the different cell layers of the SAM. Such differences were also observed in dark-grown hypocotyls and roots in promoter GUS fusions of *CESA1* and *CESA3* promoters (Persson et al., 2007). It is possible that certain internal regulatory sequences of these genes were absent in our constructs and that function at the protein level could be different in the various domains of the SAM; however, constructs that have used promoters driving the corresponding *CESA* genes fully rescue the related mutant phenotypes (Desprez et al., 2007). Thus, these data indicate that the promoters do drive *CESA* expression where it is needed.

The existence of a supracellular feedback mechanism between tissue geometry-driven physical stress that controls the orientation of MTs and, therefore, the anisotropy of cellulose in the cell wall is thought to control morphogenesis at the SAM (Sampathkumar et al., 2014b). The patterning of CMF mirrors that of MTs in the different domains of the SAM, corroborating such a model. However, such a feedback mechanism appears to be well supported only in the L1 layer, because there were some differences between MT ordering and CMF organization in the anticlinal walls of the L2 layer. The lack of correspondence between the CMF and MTs has been shown in several previous studies (Sugimoto et al., 2003; Fujita et al., 2011). One explanation for this could be that the activity of proteins such as CELLULOSE SYNTHASE INTERACTING PROTEIN 1, which associates CESA to MTs, could be differently regulated in different cell layers (Bringmann et al., 2012), although there are also other possibilities. However, the increased number of pit fields in the L2 anticlinal walls makes it difficult to determine conclusively the major alignment direction of the CMFs. Quantitative assessment of such micrographs failed with existing tools that allow for measurement of fibril anisotropy (Boudaoud et al., 2014). New tools that permit for such analysis of low-contrast images are necessary to evaluate this in a quantitative manner. Previous genetic evidence indicates that *cesa6* and *rsw1-1* mutants have disrupted MT organization in root epidermal cells (Paredes et al., 2008; Sugimoto et al., 2001). Similarly, reduced anisotropy of MTs was observed in the central domain of the SAM in the *cev1* mutant. This indicates a feedback machinery that could exist between the status of the cell wall (either chemical or physical) and MT organization. Moreover, the mutants used in this study influence different aspects of cellulose biosynthesis, with *any1* having no changes in cellulose amount but showing reduced crystallinity (Fujita et al., 2013), whereas *cev1* has been reported to have reduced levels of cellulose in roots with no changes in leaf tissue (Ellis et al., 2002). Nevertheless, in all cases, cellulose production was not completely abolished. Several other components of the cell wall, such as pectins and xyloglucans, are known to adhere and tether CMFs to each other in primary walls (Cosgrove, 2014), and protein activities, such as expansins (Fleming et al., 1997), that influence such interactions, could also have a role in SAM morphogenesis (Armezzani et al., 2018). However, the *cesa* mutants were still morphologically different from wild type, indicating that such compensatory mechanisms require an intact CMF network in the SAM.

Previous studies showed that the polar distribution of PIN1-GFP driven by the *PIN2* promoter was altered in root cells of several primary wall *cesa* mutants and in seedlings treated with pharmacological agents that disrupt cellulose synthesis (Feraru et al., 2011). Polar subdomains and circumferential distribution of PIN1-GFP and highly organized MT arrays were observed in SAMs treated with isoxaben (Heisler et al., 2010). These results were

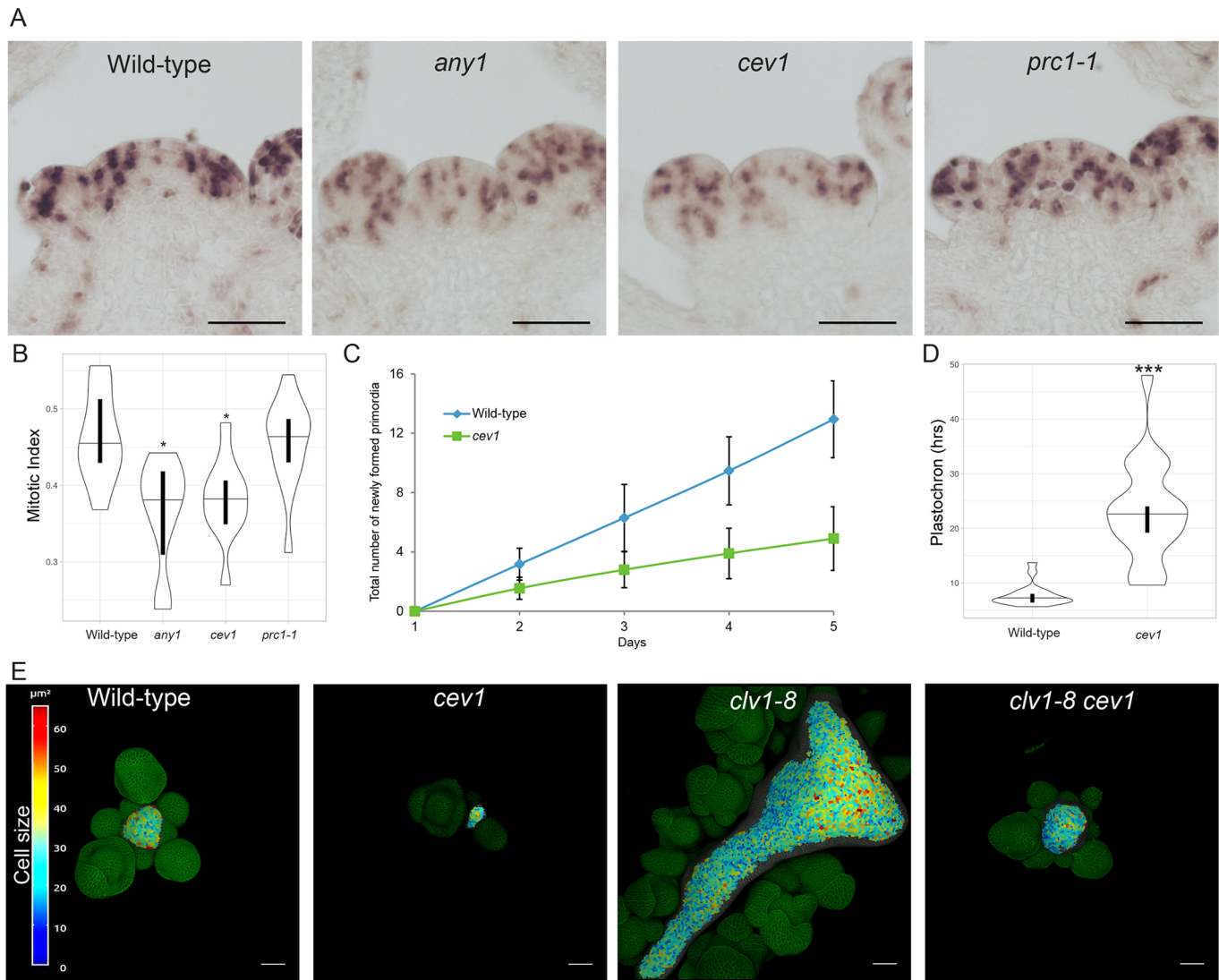


**Fig. 6. CESA influences cell growth and plastochron at the SAM.** (A) Representative images of *in situ* hybridization using *HISTONE H4* RNA probes on SAM sections of different genotypes. (B) Violin plot reflecting the distribution of the mitotic index of the genotypes. The mitotic index is defined as the ratio of cells in S phase to the total number of cells in the meristematic region (see Materials and Methods) (wild type  $n=11$ , *any1*  $n=10$ , *cev1*  $n=11$  and *prc1-1*  $n=13$  SAMs). (C) Graph showing the total number of newly formed primordia over a period of 5 days in wild type and *cev1* (error bars show s.e.m.). (D) Violin plot of plastochron obtained from primordial emergence within a 96-h period for wild type and *cev1* (wild type  $n=220$  primordia from 17 SAMs, *cev1*  $n=98$  primordia from 20 SAMs; for both C and D). (E) 3D rendered surface projection of Propidium Iodide-stained SAMs of different genotypes. Individual cells of the L1 layer are segmented and a heat map of the cell surface area is projected onto the surface. The horizontal lines in each violin plot indicate the median, whereas vertical bars indicate the 95% confidence interval for each median determined by bootstrapping. \* $P < 0.01$ , \*\*\* $P < 0.0001$  (Welch's *t*-test). Scale bars: 50  $\mu$ m in A,E.

proposed to be a consequence of increased tensional forces arising through transient perturbation of the stiffness of the cell wall, rather than a direct impact of cellulose biosynthesis on PIN1 distribution. Given that the reduction of stiffness could result in increased tension in the cell wall mutants, it is surprising that, in our experiments, MT anisotropy was reduced. Nevertheless, spatial patterning of CMFs and MTs was not different from wild type, thereby allowing proper regulation of organ emergence at the SAM. The above change could also result from the activity of the cell wall integrity response in the mutants, which could influence PIN1 levels. The *cev1* mutant was initially isolated as a mutant having increased activity of both the jasmonate and ethylene signaling pathways (Ellis et al., 2002; Ellis and Turner, 2001). This particular imbalance could also contribute to the above-mentioned tissue-level and subcellular phenotypes in the SAM.

Regardless, the phenotypic data from the SAM point toward impaired growth and reduced cell division as reflected in the reduced mitotic index, which could further impact organogenesis in the tested mutants. This is substantiated by the suppression of the fasciation phenotype of *clv1-8* when combined with a *cesa* mutant. The observation that cell size was not impacted in *cesa* mutants further suggests that cells would require more time to reach a certain cell size threshold, which then acts as an important step for the cell to enter mitosis (Willis et al., 2016). Supportive of this, previous studies on a temperature-sensitive mutant of *CESA* showed that cell expansion rapidly ceases at restrictive temperatures in roots (Sugimoto et al., 2001). These effects were proven to be under the influence of the plasma membrane receptor-like kinase THESEUS1, which acts as a cell wall integrity sensor in plants with perturbed cellulose synthesis (Hématy et al., 2007). In



addition, isoxaben-induced cellulose perturbation impacts the expression of genes associated with cell cycle progression in a cytokinin-dependent fashion, hindering root growth (Gigli-Bisceglia et al., 2018). It is also plausible that feedback from mechanical signals via cell wall integrity sensing could influence the growth of cells, thereby impacting cell proliferation rates. However, the exact mechanism involved remains to be determined. Overall, we conclude that deficiencies in cellulose biosynthesis influence the growth, morphology and cell wall mechanics of the SAM.

## MATERIALS AND METHODS

### Plant material

*MBD-GFP*, *any1*, *cevl*, *prc1-1*, *clv1-8*, *pPIN1:PIN1:GFP* and *pTCS:GFP* are described in the literature (Marc et al., 1998; Fujita et al., 2013; Ellis et al., 2002; Fagard et al., 2000; Nimchuk et al., 2015; Benková et al., 2003; Zurcher et al., 2013; Reddy et al., 2004). To generate *pCESA1:TdN7* and *pCESA3:2XGFPN7*, we first amplified 4.5 kb of the region upstream of the *CESA1* (AT4G32410) translation initiation ATG, *TdTOMATO*, harboring a nuclear targeting sequence and a 1.5-kb downstream sequence of the stop codon for *pCESA1:TdN7* with primers having complementary ends that facilitate homology-based recombination between them. In a similar fashion, 3.2 kb upstream of *CESA3* (AT5G05170), a *2XGFP* linked to a nuclear targeting sequence and 1.5 kb downstream of the gene was amplified. The amplified fragments were combined by means of a single-step direction cloning process into minimal T-DNA vectors pMOA34 and pMOA33 (Barrell and Conner, 2006) to obtain *pCESA1:TdN7* and *pCESA3:2XGFPN7*, respectively, by means of In-Fusion Cloning (Takara Bio). These constructs were transferred to *Col-0* plants by *Agrobacterium*-mediated transformation and selected for antibiotic resistance and presence of fluorescence. A minimum of ten individual T1 plants was screened and checked for consistency of the observed expression pattern. Mutant combinations of *cevl clv1-8* and incorporation of fluorescent reporters *MBD-GFP*, *pPIN1:PIN1:GFP* and *pTCS:GFP* into the *cevl* mutant background were done by crossing.

### Genotyping of mutant plants

Both *cevl* and *clv1-8* were genotyped using a dCAPS primer generated via the dCAPS Finder 2.0 web tool (Neff et al., 2002). The primers were as follows: *cevl* forward primer (TTGAGAGGTTTAGATGGGATTCAAG-GACCTGTATATGTCGGAACCT) and reverse primer (ATCCCCTCCC-CTGGATCAAT), with mutants providing a 315-bp fragment when restricted with MseI; and *clv1-8* forward primer (GAAGCTTTGAGGG-ATTTCTCCGGTTAACTGATTGATTGATAACT) and reverse primer (CCACCGGAGTTCGGTGGTTTAAACAAAGC), with mutants producing a 190-bp fragment when restricted with XhoI. The fragments were resolved on 3.5% agarose gel.

### Plant growth, confocal imaging and analysis

Plants used for laser scanning confocal microscopy and FESEM were grown in short-day conditions (8 h light) for a period of 4 weeks and then transferred to long-day conditions (16 h light). The *clv1-8 cevl* double mutants were phenotyped under continuous light conditions. The plants were allowed to bolt and, upon reaching a height of 2 cm, the main stem was dissected along with the SAM and flowers. The older flower buds were carefully removed under a dissecting microscope using sharp forceps to expose the SAM for imaging. Morphological observations of the SAM were performed after staining the SAM with 1 mg/ml of Propidium Iodide solution for 2 min. SAMs were imaged with a Zeiss 780 or Leica SP8 confocal microscope with a 40× water-dipping objective, and Z-stacks of SAMs with 0.5 µm intervals were obtained for 3D reconstruction. Images were processed with FIJI (<https://fiji.sc/>) or Imaris (Bitplane AG). Maps of cell surface area and SAM curvature were generated using MorphographX (Barbier de Reuille et al., 2014). Nematic tensors of MT arrays for individual cells were obtained using FibrilTool (Boudaoud et al., 2014). Measurement of the divergent angle between siliques was performed as previously described using a custom-made device on fully grown plants (Landrein

et al., 2015). SAM size was measured by quantifying the cross-section between primordia on fixed and sectioned SAMs up to five cell layers deep. Projection images were generated from confocal Z stacks of both *pPIN1:PIN1:GFP* and *pTCS:GFP* and total fluorescent intensity was measured in the region of interest using FIJI. Statistical analysis and generation of violin and box plots were done using PlotsOfData (Postma and Goedhart, 2019) or R/shiny (Spitzer et al., 2014) web tools.

### Cell wall preparation for field emission scanning electron microscopy

The SAM was excised from the inflorescence stems and processed for FESEM observation as described previously (Sugimoto et al., 2000; Fujita and Wasteneys, 2014). Excised SAMs were fixed in 0.5% (v/v) glutaraldehyde and 4% formaldehyde in PME buffer (25 mM PIPES, 0.5 mM MgSO<sub>4</sub> and 2.5 mM EGTA, pH 7.2) for 20 min under vacuum and for another 40 min without vacuum. Samples were rinsed three times for 10 min, each time in PME buffer, and were cryoprotected in 25% and 50% (v/v) dimethyl sulfoxide (DMSO) in PME buffer for 10 min each. Samples were frozen in liquid nitrogen and the surface of the meristem was sliced off using a cryo-ultramicrotome (Ultracut T ultramicrotome with Leica EM FCS attachment, Leica). The remaining portion of the specimen was thawed in 50% (v/v) DMSO in PME buffer and rinsed in PME buffer. Cytoplasmic materials were extracted by incubating them in a 1% NaCl solution for 10 min, followed by three 10-min washes in distilled water. Samples were incubated with 2% OsO<sub>4</sub> for 1 h and washed in distilled water three times for 10 min. After gradual dehydration with an ethanol series, samples were critical point-dried (Autosamdri 815B Critical Point Dryer, Tousimis) and coated with Pt/Pd (80/20) at 40 mA to a 5-nm thickness (High-Resolution Sputter Coater 208R, Cressington). Cellulose microfibrils were observed with a Hitachi S4700 SEM set at 3 kV and 10 µA current using an upper detector with a 5-mm working distance.

### Pharmacological treatments and cell ablation

Dissected SAMs were transferred to plates containing 2.2 g l<sup>-1</sup> Murashige and Skoog (MS) medium, Gamborg B5 vitamins (Duchefa), and 1% w/v agar. The SAMs were immersed either in 40 µM isoxaben (36138 Sigma) or 0.1% cellulase (C1184 Sigma) for 24 h along with controls containing equivalent volumes of DMSO. For each experiment, at least ten SAMs were treated and analyzed either with a confocal microscope or AFM. The ablations were performed on six SAMs using a needle as described previously (Uyttewaal et al., 2012) and imaged every hour for a period of 5 h.

### Atomic force microscopy

The mutant SAMs were freshly dissected from the inflorescence, immobilized on glass slides and surrounded by stiff low-melting temperature agarose. Pharmacological treatments of the SAMs were performed for a period of 24 h by immersing the dissected SAMs placed on growth media with the reagents before mounting on glass slides for measurement. To extract the anticlinal wall mechanical properties, the maximum indentation was set at 500 nM. The cantilever used was a NanoWorld (Nanosensors) SD-Sphere-FM-S-10 tip with a spring constant of 2.8 N/m (the one used was estimated to be 9.5 N/m) with silicon point probe tips with a 500-nm radius.

All AFM experiments were performed as previously described on plasmolyzed SAMs (Peaucelle et al., 2011). Briefly, the stiffness of samples was determined as follows: an AFM cantilever loaded with a spherical tip was used to indent the sample over a 80×80 µm<sup>2</sup> area, within which 80×80 measurements were made resulting in 6400 force-indentation experiments; each force-indentation experiment was treated with a Hertzian indentation model to extract the apparent Young's modulus ( $E_A$ ); each pixel in the resulting stiffness map represented the apparent Young's modulus from one force-indentation point. The  $E_A$  was calculated using JPK Data Processing software (ver. Spm - 4.0.23, JPK Instruments AG), which allows for a more standardized analysis than the estimation of the  $E_A$  using a standard Hertzian contact model (Peaucelle et al., 2011). Only the retraction curve was used in our analyses as is typically the case in nano-indentation experiments. Similar stiffness differences as reported earlier were also observed when using the deformation curve (data not shown), yet this measurement appeared more

sensitive to the topography, leading to aberrant measurements at meristem edges. The best fit was obtained using a Hertzian model with a tip radius of 500 nm. A Poisson ratio of 0.5 was assumed for the material. Periclinal wall measurements were selected using a Matlab interface.

### Quantification of mitotic index

RNA *in situ* hybridization of SAMs using HISTONE H4 RNA antisense probes and quantification of mitotic index were performed as described previously (Geier et al., 2008; Maier et al., 2009). To determine the threshold, the mean intensity of unstained regions of the SAM was measured and subtracted with four times the value of the standard deviation. This allowed for correction of differences in staining intensities between the different sections and slides as well as differences in sample illumination. The mitotic index was then calculated as the ratio between the total number of pixels of the meristematic region (area between the primordia and up to five cell layers deep) below the threshold to the total number of pixels of the meristematic region. The five most central sections of the SAM were considered for quantification.

### Estimation of plastochron

The number of visible primordia at the SAM was measured every day for 5 days using a dissecting microscope. A reference was created on the first day by removing one or two consecutive stage two or three primordia. To control for potential stress induced by tweezer manipulation, control plants were observed only on the first and last day.

### Acknowledgements

We thank Olivier Hamant for critical reading and comments on the manuscript; René Schneider for suggesting the use of PlotSofData for generation of violin plots; Paul Tarr and all members of the Meyerowitz lab at the California Institute of Technology for helpful discussions on the topic. We also thank the University of British Columbia Bioimaging Facility for access to the scanning electron microscope.

### Competing interests

The authors declare no competing or financial interests.

### Author contributions

Conceptualization: A.S., E.M.M.; Methodology: A.S., A.P., M.F., C.S., G.O.W.; Validation: A.S., M.F., C.S.; Formal analysis: A.S., A.P., M.F., C.S., S.P., G.O.W., E.M.M.; Investigation: A.S., A.P., M.F., C.S., S.P., G.O.W., E.M.M.; Resources: A.S., S.P., G.O.W., E.M.M.; Data curation: A.S., A.P., M.F., C.S.; Writing - original draft: A.S.; Writing - review & editing: A.S., C.S., S.P., G.O.W., E.M.M.; Visualization: A.S., A.P., M.F.; Supervision: G.O.W., E.M.M.; Funding acquisition: A.S., E.M.M.

### Funding

A.S. is supported by the Max-Planck-Gesellschaft. C.S. is supported by a Gatsby Charitable Foundation fellowship (GAT3395/DAA). S.P. was supported by an ARC Future Fellowship grant (FT160100218). G.O.W. was supported by a Natural Sciences and Engineering Research Council of Canada Discovery Grant (2014-06080). E.M.M. is a Howard Hughes Medical Institute investigator. Deposited in PMC for release after 12 months.

### Supplementary information

Supplementary information available online at <http://dev.biologists.org/lookup/doi/10.1242/dev.179036.supplemental>

### References

- Armezzani, A., Abad, U., Ali, O., Andres Robin, A., Vachez, L., Larrieu, A., Mellerowicz, E. J., Taconnat, L., Battu, V., Stanislas, T. et al. (2018). Transcriptional induction of cell wall remodelling genes is coupled to microtubule-driven growth isotropy at the shoot apex in Arabidopsis. *Development* **145**, dev162255. doi:10.1242/dev.162255
- Barbier de Reuille, P., Routier-Kierzkowska, A.-L., Kierzkowski, D., Bassel, G. W., Schüpbach, T., Tauriello, G., Bajpai, N., Strauss, S., Weber, A., Kiss, A., et al. (2015). MorphoGraphX: A platform for quantifying morphogenesis in 4D. *eLife* **4**, e05864. doi:10.7554/eLife.05864
- Barrell, P. J. and Conner, A. J. (2006). Minimal T-DNA vectors suitable for agricultural deployment of transgenic plants. *BioTechniques* **41**, 708-710. doi:10.2144/000112306
- Barton, M. K. (2010). Twenty years on: the inner workings of the shoot apical meristem, a developmental dynamo. *Dev. Biol.* **341**, 95-113. doi:10.1016/j.ydbio.2009.11.029
- Benková, E., Michniewicz, M., Sauer, M., Teichmann, T., Seifertová, D., Jürgens, G. and Friml, J. (2003). Local, efflux-dependent auxin gradients as a common module for plant organ formation. *Cell* **115**, 591-602. doi:10.1016/S0092-8674(03)00924-3
- Boudaoud, A., Burian, A., Borowska-Wykręć, D., Uyttewaald, M., Wrzalić, R., Kwiatkowska, D. and Hamant, O. (2014). FibrilTool, an ImageJ plug-in to quantify fibrillar structures in raw microscopy images. *Nat. Protoc.* **9**, 457-463. doi:10.1038/nprot.2014.024
- Braybrook, S. A. and Peaucelle, A. (2013). Mechano-chemical aspects of organ formation in Arabidopsis thaliana: the relationship between auxin and pectin. *PLoS ONE* **8**, e57813. doi:10.1371/journal.pone.0057813
- Bringmann, M., Li, E., Sampathkumar, A., Kocabek, T., Hauser, M.-T. and Persson, S. (2012). POM-POM2/cellulose synthase interacting1 is essential for the functional association of cellulose synthase and microtubules in Arabidopsis. *Plant Cell* **24**, 163-177. doi:10.1105/tpc.111.093575
- Cosgrove, D. J. (2014). Re-constructing our models of cellulose and primary cell wall assembly. *Curr. Opin. Plant Biol.* **22**, 122-131. doi:10.1016/j.pbi.2014.11.001
- Desprez, T., Juraniec, M., Crowell, E. F., Jouy, H., Pochylova, Z., Parcy, F., Hofte, H., Gonneau, M. and Vernhettes, S. (2007). Organization of cellulose synthase complexes involved in primary cell wall synthesis in Arabidopsis thaliana. *Proc. Natl. Acad. Sci. USA* **104**, 15572-15577. doi:10.1073/pnas.0706569104
- Ellis, C. and Turner, J. G. (2001). The Arabidopsis mutant cev1 has constitutively active jasmonate and ethylene signal pathways and enhanced resistance to pathogens. *Plant Cell* **13**, 1025-1033. doi:10.1105/tpc.13.5.1025
- Ellis, C., Karafyllidis, I., Wasternack, C. and Turner, J. G. (2002). The Arabidopsis mutant cev1 links cell wall signaling to jasmonate and ethylene responses. *Plant Cell* **14**, 1557-1566. doi:10.1105/tpc.002022
- Fagard, M., Desnos, T., Desprez, T., Goubet, F., Refregier, G., Mouille, G., Mccann, M., Rayon, C., Vernhettes, S. and Hofte, H. (2000). PROCUSTE1 encodes a cellulose synthase required for normal cell elongation specifically in roots and dark-grown hypocotyls of Arabidopsis. *Plant Cell* **12**, 2409-2424. doi:10.1105/tpc.12.12.2409
- Feraru, E., Feraru, M. I., Kleine-Vehn, J., Martinière, A., Mouille, G., Vanneste, S., Vernhettes, S., Runions, J. and Friml, J. (2011). PIN polarity maintenance by the cell wall in Arabidopsis. *Curr. Biol.* **21**, 338-343. doi:10.1016/j.cub.2011.01.036
- Fleming, A. J., McQueen-Mason, S., Mandel, T. and Kuhlemeier, C. (1997). Induction of Leaf Primordia by the Cell Wall Protein Expansin. *Science* **276**, 1415. doi:10.1126/science.276.5317.1415
- Fujita, M. and Wasteneys, G. O. (2014). A survey of cellulose microfibril patterns in dividing, expanding, and differentiating cells of Arabidopsis thaliana. *Protoplasma* **251**, 687-698. doi:10.1007/s00709-013-0571-2
- Fujita, M., Himmelspach, R., Hocart, C. H., Williamson, R. E., Mansfield, S. D. and Wasteneys, G. O. (2011). Cortical microtubules optimize cell-wall crystallinity to drive unidirectional growth in Arabidopsis. *The Plant Journal* **66**, 915-928. doi:10.1111/j.1365-3113X.2011.04552.x
- Fujita, M., Himmelspach, R., Ward, J., Whittington, A., Hasenbein, N., Liu, C., Truong, T. T., Galway, M. E., Mansfield, S. D., Hocart, C. H. et al. (2013). The anisotropy1 D604N mutation in the Arabidopsis cellulose synthase1 catalytic domain reduces cell wall crystallinity and the velocity of cellulose synthase complexes. *Plant Physiol.* **162**, 74-85. doi:10.1104/pp.112.211565
- Geier, F., Lohmann, J. U., Gerstung, M., Maier, A. T., Timmer, J. and Fleck, C. (2008). A quantitative and dynamic model for plant stem cell regulation. *PLoS ONE* **3**, e3553. doi:10.1371/journal.pone.0003553
- Gigli-Biscaglia, N., Engelsdorf, T., Strnad, M., Vaahtera, L., Khan, G. A., Yamoune, A., Alipanah, L., Novák, O., Persson, S., Hejatk, J. and Hamann, T. (2018). Cell wall integrity modulates Arabidopsis thaliana cell cycle gene expression in a cytokinin- and nitrate reductase-dependent manner. *Development* **145**, dev166678. doi:10.1242/dev.166678
- Griffiths, J. S., Sola, K., Kushwaha, R., Lam, P., Tateno, M., Young, R., Voiniciuc, C., Dean, G., Mansfield, S. D., Debolt, S. et al. (2015). Unidirectional movement of cellulose synthase complexes in Arabidopsis seed coat epidermal cells deposit cellulose involved in mucilage extrusion, adherence, and ray formation. *Plant Physiol.* **168**, 502-520. doi:10.1104/pp.15.00478
- Hamant, O., Heisler, M. G., Jonsson, H., Krupinski, P., Uyttewaald, M., Bokov, P., Corson, F., Sahlén, P., Boudaoud, A., Meyerowitz, E. M. et al. (2008). Developmental patterning by mechanical signals in Arabidopsis. *Science* **322**, 1650-1655. doi:10.1126/science.1165594
- Heisler, M. G., Hamant, O., Krupinski, P., Uyttewaald, M., Ohno, C., Jönsson, H., Traas, J. and Meyerowitz, E. M. (2010). Alignment between PIN1 polarity and microtubule orientation in the shoot apical meristem reveals a tight coupling between morphogenesis and auxin transport. *PLoS Biol.* **8**, e1000516. doi:10.1371/journal.pbio.1000516
- Hématy, K., Sado, P.-E., VAN Tuinen, A., Rochange, S., Desnos, T., Balzergue, S., Pelletier, S., Renou, J.-P. and Höfte, H. (2007). A receptor-like kinase mediates the response of Arabidopsis cells to the inhibition of cellulose synthesis. *Curr. Biol.* **17**, 922-931. doi:10.1016/j.cub.2007.05.018
- Landrein, B., Refahi, Y., Besnard, F., Hervieux, N., Mirabet, V., Boudaoud, A., Vernoux, T. and Hamant, O. (2015). Meristem size contributes to the robustness of phyllotaxis in Arabidopsis. *J. Exp. Bot.* **66**, 1317-1324. doi:10.1093/jxb/eru482



- Maier, A. T., Stehling-Sun, S., Wollmann, H., Demar, M., Hong, R. L., Haubeiss, S., Weigel, D. and Lohmann, J. U. (2009). Dual roles of the bZIP transcription factor PERANTHIA in the control of floral architecture and homeotic gene expression. *Development* **136**, 1613. doi:10.1242/dev.033647
- Marc, J., Granger, C. L., Brincat, J., Fisher, D. D., Kao, T.-H., McCubbin, A. G. and Cyr, R. J. (1998). A GFP-MAP4 reporter gene for visualizing cortical microtubule rearrangements in living epidermal cells. *Plant Cell* **10**, 1927-1939. doi:10.2307/3870914
- Mcfarlane, H. E., Döring, A. and Persson, S. (2014). The cell biology of cellulose synthesis. *Annu. Rev. Plant Biol.* **65**, 69-94. doi:10.1146/annurev-arplant-050213-040240
- Mendu, V., Griffiths, J. S., Persson, S., Stork, J., Downie, A. B., Voiniciuc, C., Haughn, G. W. and Debolt, S. (2011). Subfunctionalization of cellulose synthases in seed coat epidermal cells mediates secondary radial wall synthesis and mucilage attachment. *Plant Physiol.* **157**, 441-453. doi:10.1104/pp.111.179069
- Neff, M. M., Turk, E. and Kalishman, M. (2002). Web-based primer design for single nucleotide polymorphism analysis. *Trends Genet.* **18**, 613-615. doi:10.1016/S0168-9525(02)02820-2
- Nimchuk, Z. L., Zhou, Y., Tarr, P. T., Peterson, B. A. and Meyerowitz, E. M. (2015). Plant stem cell maintenance by transcriptional cross-regulation of related receptor kinases. *Development* **142**, 1043-1049. doi:10.1242/dev.119677
- Paredes, A. R., Somerville, C. R. and Ehrhardt, D. W. (2006). Visualization of cellulose synthase demonstrates functional association with microtubules. *Science* **312**, 1491-1495. doi:10.1126/science.1126551
- Paredes, A. R., Persson, S., Ehrhardt, D. W. and Somerville, C. R. (2008). Genetic evidence that cellulose synthase activity influences microtubule cortical array organization. *Plant Physiol.* **147**, 1723. doi:10.1104/pp.108.120196
- Peaucelle, A., Braybrook, S. A., Le Guillou, L., Bron, E., Kuhlmeier, C. and Höfte, H. (2011). Pectin-induced changes in cell wall mechanics underlie organ initiation in Arabidopsis. *Curr. Biol.* **21**, 1720-1726. doi:10.1016/j.cub.2011.08.057
- Persson, S., Paredes, A., Carroll, A., Palsdottir, H., Doblin, M., Poindexter, P., Khitrov, N., Auer, M. and Somerville, C. R. (2007). Genetic evidence for three unique components in primary cell-wall cellulose synthase complexes in Arabidopsis. *Proc. Natl. Acad. Sci. USA* **104**, 15566-15571. doi:10.1073/pnas.0706592104
- Postma, M. and Goedhart, J. (2019). PlotsOfData—A web app for visualizing data together with their summaries. *PLoS Biol.* **17**, e3000202. doi:10.1371/journal.pbio.3000202
- Reddy, G. V., Heisler, M. G., Ehrhardt, D. W. and Meyerowitz, E. M. (2004). Real-time lineage analysis reveals oriented cell divisions associated with morphogenesis at the shoot apex of Arabidopsis thaliana. *Development* **131**, 4225. doi:10.1242/dev.01261
- Sampathkumar, A., Krupinski, P., Wightman, R., Milani, P., Berquand, A., Boudaoud, A., Hamant, O., Jönsson, H. and Meyerowitz, E. M. (2014a). Subcellular and supracellular mechanical stress prescribes cytoskeleton behavior in Arabidopsis cotyledon pavement cells. *Elife* **3**, e01967. doi:10.7554/eLife.01967
- Sampathkumar, A., Yan, A., Krupinski, P. and Meyerowitz, E. M. (2014b). Physical forces regulate plant development and morphogenesis. *Curr. Biol.* **24**, R475-R483. doi:10.1016/j.cub.2014.03.014
- Sassi, M., Ali, O., Boudon, F., Cloarec, G., Abad, U., Cellier, C., Chen, X., Gilles, B., Milani, P., Firml, J. et al. (2014). An auxin-mediated shift toward growth isotropy promotes organ formation at the shoot meristem in Arabidopsis. *Curr. Biol.* **24**, 2335-2342. doi:10.1016/j.cub.2014.08.036
- Schoof, H., Lenhard, M., Haecker, A., Mayer, K. F. X., Jürgens, G. and Laux, T. (2000). The stem cell population of Arabidopsis shoot meristems is maintained by a regulatory loop between the CLAVATA and WUSCHEL genes. *Cell* **100**, 635-644. doi:10.1016/S0092-8674(00)80700-X
- Spitzer, M., Wildenhain, J., Rappsilber, J. and Tyers, M. (2014). BoxPlotR: a web tool for generation of box plots. *Nat. Methods* **11**, 121. doi:10.1038/nmeth.2811
- Sugimoto, K., Williamson, R. E. and Wasteneys, G. O. (2000). New techniques enable comparative analysis of microtubule orientation, wall texture, and growth rate in intact roots of Arabidopsis. *Plant Physiol.* **124**, 1493-1506. doi:10.1104/pp.124.4.1493
- Sugimoto, K., Williamson, R. E. and Wasteneys, G. O. (2001). Wall architecture in the cellulose-deficient rsw1 mutant of Arabidopsis thaliana: Microfibrils but not microtubules lose their transverse alignment before microfibrils become unrecognizable in the mitotic and elongation zones of roots. *Protoplasma* **215**, 172-183. doi:10.1007/BF01280312
- Sugimoto, K., Himmelspach, R., Williamson, R. E. and Wasteneys, G. O. (2003). Mutation or drug-dependent microtubule disruption causes radial swelling without altering parallel cellulose microfibril deposition in Arabidopsis root cells. *Plant Cell* **15**, 1414. doi:10.1105/tpc.011593
- Uyttewaal, M., Burian, A., Alim, K., Landrein, B. T., Borowska-Wykręć, D., Dedieu, A., Peaucelle, A., Ludynia, M., Traas, J., Boudaoud, A. et al. (2012). Mechanical stress acts via katanin to amplify differences in growth rate between adjacent cells in Arabidopsis. *Cell* **149**, 439-451. doi:10.1016/j.cell.2012.02.048
- Watanabe, Y., Meents, M. J., McDonnell, L. M., Barkwill, S., Sampathkumar, A., Cartwright, H. N., Demura, T., Ehrhardt, D. W., Samuels, A. L. and Mansfield, S. D. (2015). Visualization of cellulose synthases in Arabidopsis secondary cell walls. *Science* **350**, 198-203. doi:10.1126/science.aac7446
- Willis, L., Refahi, Y., Wightman, R., Landrein, B., Teles, J., Huang, K. C., Meyerowitz, E. M. and Jönsson, H. (2016). Cell size and growth regulation in the Arabidopsis thaliana apical stem cell niche. *Proc. Natl. Acad. Sci. USA* **113**, E8238. doi:10.1073/pnas.1616768113
- Yanagisawa, M., Desyatova, A. S., Belteton, S. A., Mallery, E. L., Turner, J. A. and Szymanski, D. B. (2015). Patterning mechanisms of cytoskeletal and cell wall systems during leaf trichome morphogenesis. *Nat. Plants* **1**, 15014. doi:10.1038/nplants.2015.14
- Yang, W., Schuster, C., Beahan, C. T., Charoensawan, V., Peaucelle, A., Bacic, A., Doblin, M. S., Wightman, R. and Meyerowitz, E. M. (2016). Regulation of meristem morphogenesis by cell wall synthases in Arabidopsis. *Curr. Biol.* **26**, 1404-1415. doi:10.1016/j.cub.2016.04.026
- Zurcher, E., Tavor-Deslex, D., Lituiev, D., Enkerli, K., Tarr, P. T. and Muller, B. (2013). A robust and sensitive synthetic sensor to monitor the transcriptional output of the cytokinin signaling network in planta. *Plant Physiol.* **161**, 1066-1075. doi:10.1104/pp.112.211763

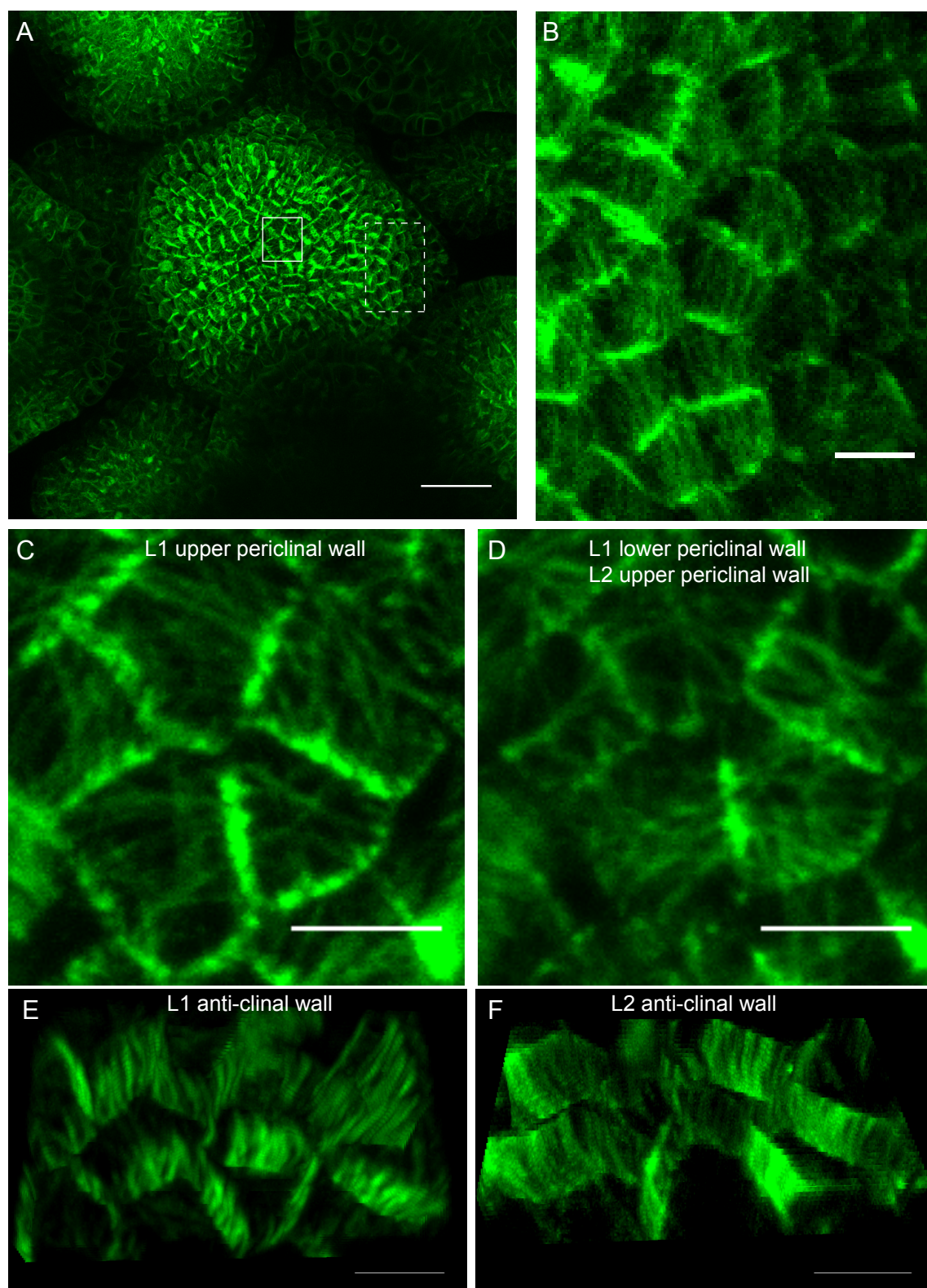


### Figure S1: Microtubule organization at the shoot apical meristem

Maximum intensity projection of microtubule organization in the L1 layer of shoot apical meristem (A). Scale bar 50 μm. Aligned microtubule arrays observed on the upper periclinal face of the margin domain (insert dotted box in A) (B). Random organization of microtubules observed on the periclinal face of central domain cells (insert box in A) (C). Projection images show disorganized microtubule arrays found in the lower periclinal face of the cells in the L1 and upper periclinal face of cells in L2 layer of the central domain (D). 3D lateral view of longitudinally aligned microtubules in L1 (E) and L2 (F) layers along the anticlinal face of cells in the central domain. Scale bars 5 μm



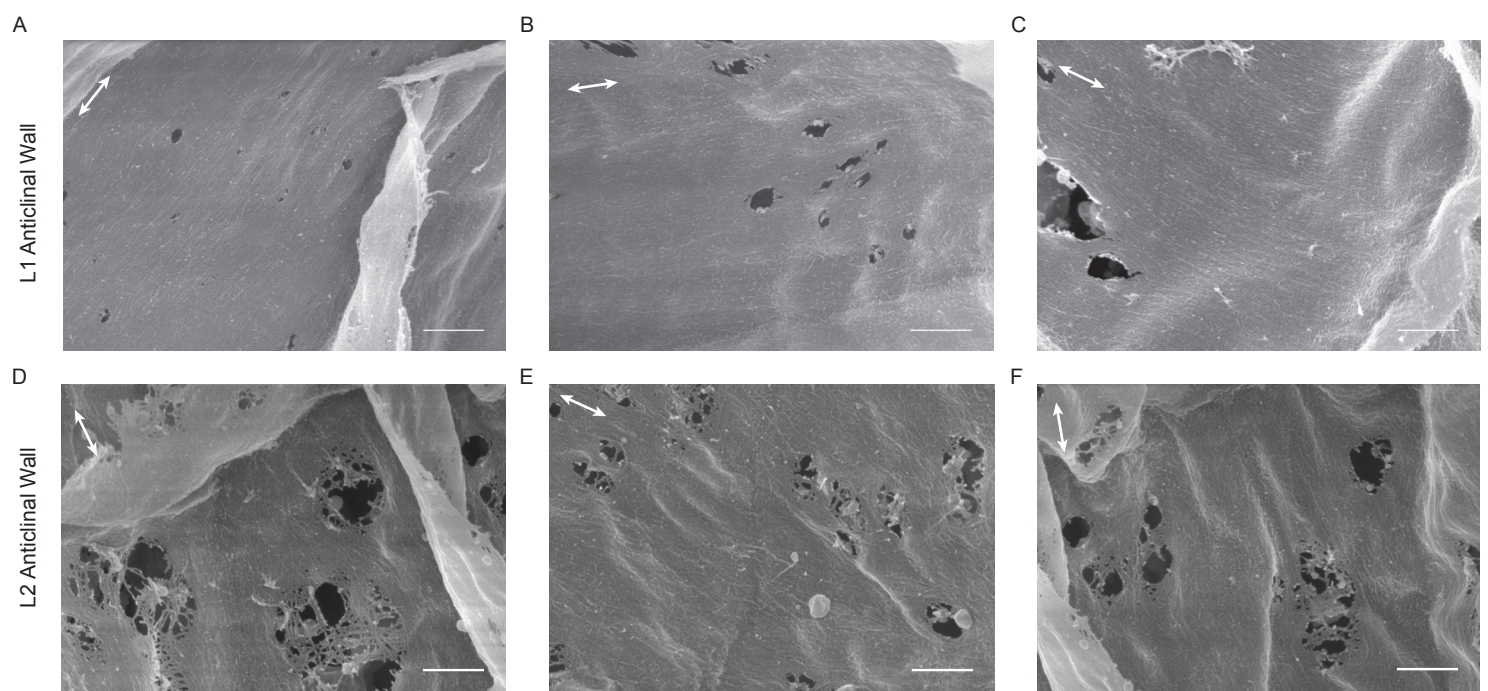


**Figure S2: Cellulose microfibril orientation at the anticlinal walls**

Longitudinal sections of cells in the central domain of shoot apical meristem. Representative images of cellulose microfibril orientations along the anticlinal wall in L1 (A-C) and L2 (D-F) cells. White lines with double arrows indicates cells longitudinal axis. Scale bars 500 nm.

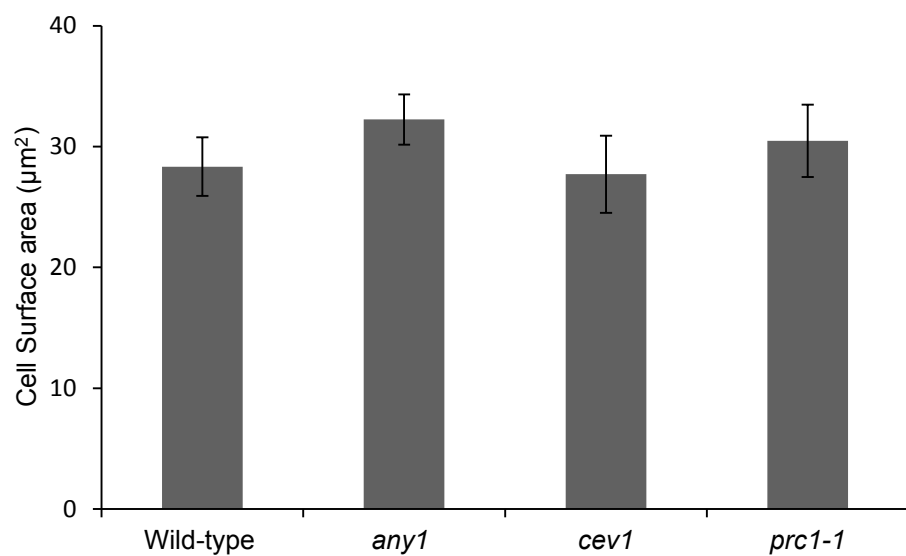


**Figure S3: Cell size is unaffected in cellulose synthase mutants**

Average cell size in the central zone cells of the different cellulose synthase mutants (N= Cells/shoot apical meristems, Wild-type=253/3, *any1*=199/3, *cev1*=145/4 and *prc1-1*=118/3)



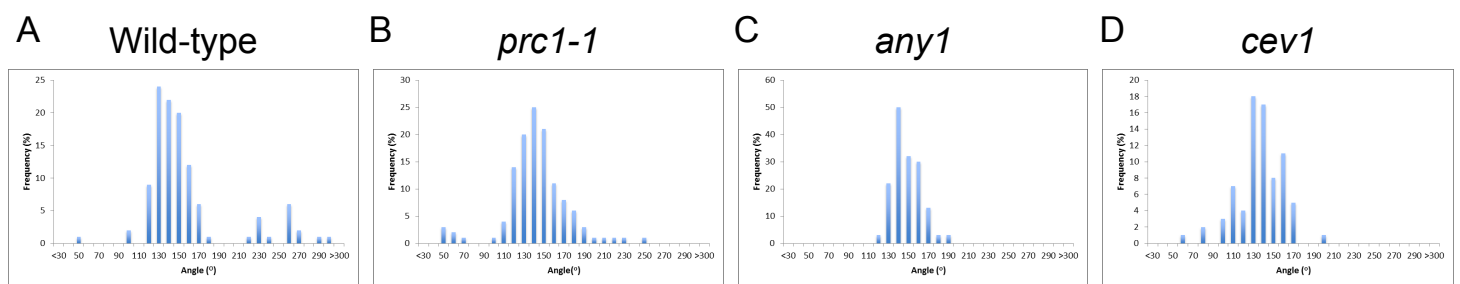


**Figure S4: Post meristematic phyllotactic patterning in cellulose synthase mutants**  
 Distribution of frequencies of divergence angles between successive siliques (A) in wild-type (n=113, 9 plants), (B) *prc1-1* (n=124, 8 plants), (C) *any1* (n=156, 8 plants) and (D) *cev1* (n=77, 7 plants).

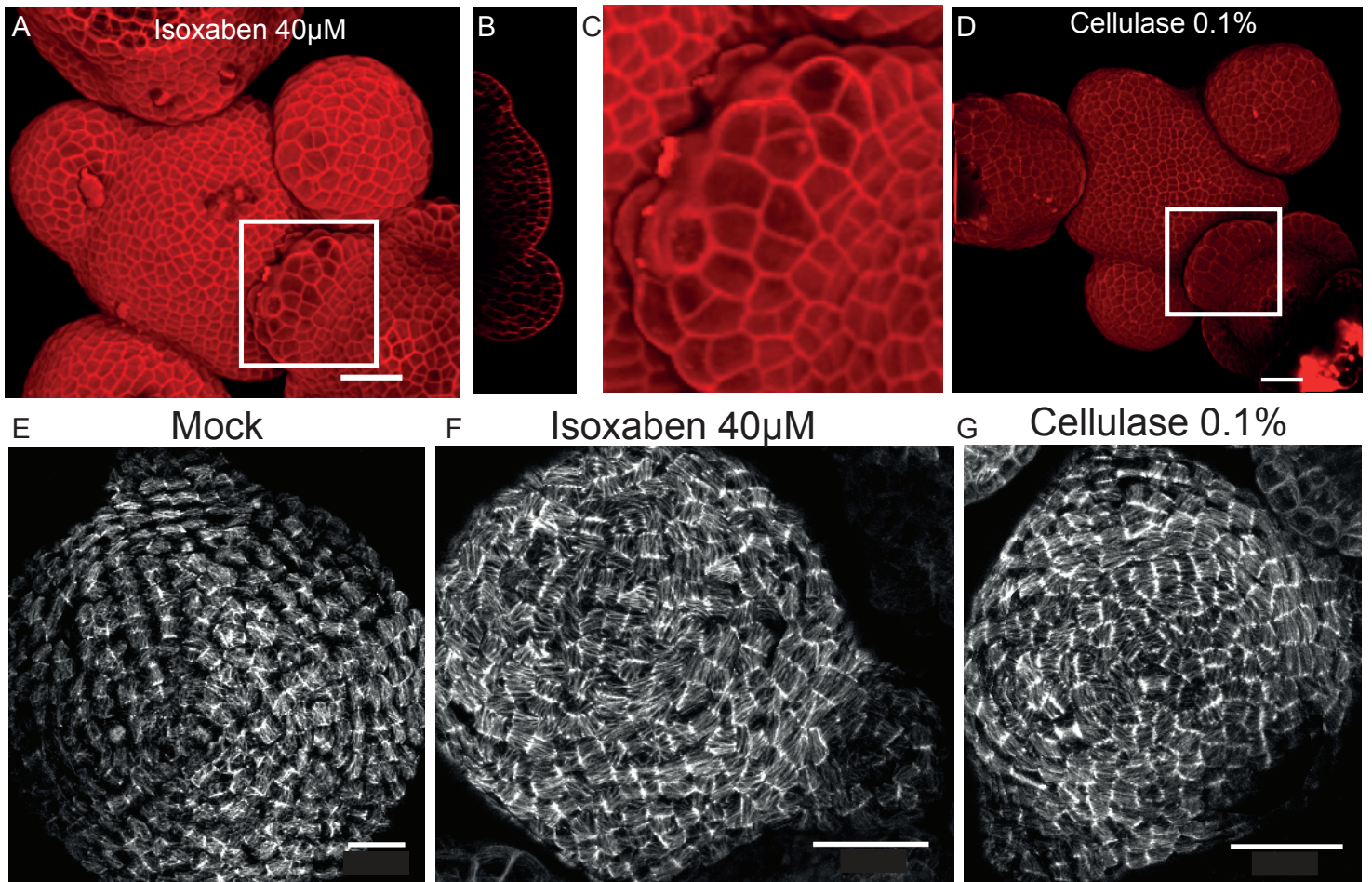


**Figure S5: Pharmacological and enzymatic disruption of cellulose:**

75 hrs treatment of wild-type shoot apical meristem with 40 μM isoxaben (A) Orthogonal view along the center of the shoot apical meristem (B) Enlarged image showing swelling of young sepal primordia insert (white box) in A (C) and 0.1% cellulase (D) treated shoot apical meristem for a period of 75 hrs. Swelling of young sepal primordia insert (white box). Microtubule organization in the L1 layer of MBD GFP lines expressing shoot apical meristem treated for 24 hrs with DMSO control (E) 40 μM isoxaben (F) and 0.1% cellulase (G). Scale bars 25 μm.



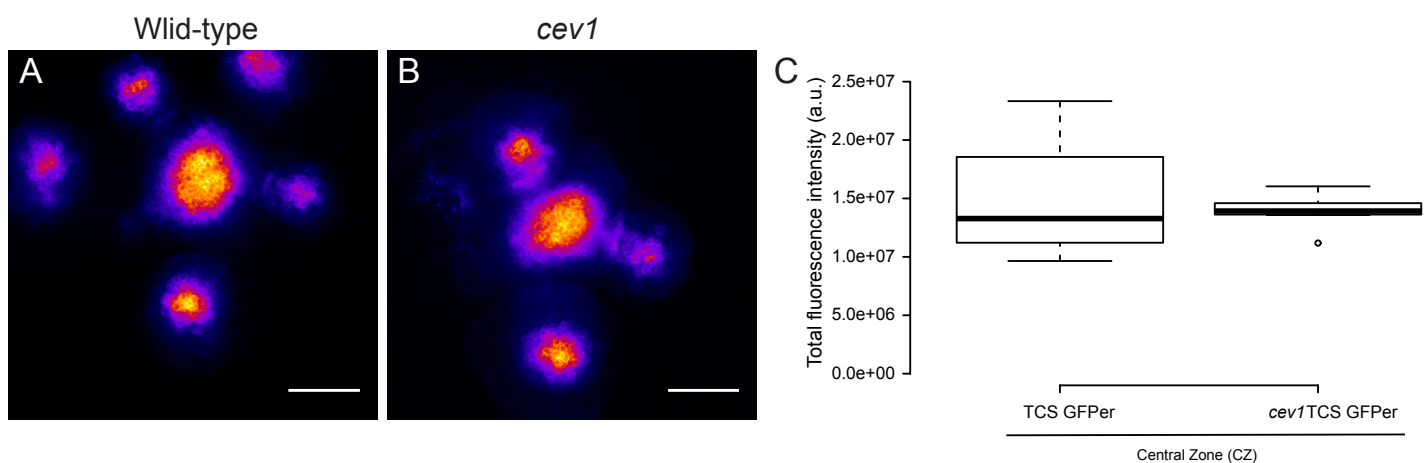


**Figure S6: Cytokinin status in wild-type and *cev1* mutant meristem**

Sum intensity projection of *pTCS:GfPer* wild-type (A) and *cev1* (B). Box plots of total fluorescence intensity obtained from cells of the central zone (enclosure 25  $\mu$ m radius). (Wild-type N=5, *cev1* N=4 shoot apical meristems) (C). Scale bars 50  $\mu$ m. Center lines in box plots show the medians; box limits indicate the 25th and 75th percentiles as determined by R software; whiskers extend 1.5 times the interquartile range from the 25th and 75th percentiles, outliers are represented by dots.